

Toward an AI Physicist for Unsupervised Learning

Tailin Wu, Max Tegmark

Dept. of Physics, Massachusetts Institute of Technology, Cambridge, MA 02139; tailin@mit.edu

(Dated: December 13, 2021)

We investigate opportunities and challenges for improving unsupervised machine learning using four common strategies with a long history in physics: divide-and-conquer, Occam’s Razor, unification, and lifelong learning. Instead of using one model to learn everything, we propose a novel paradigm centered around the learning and manipulation of *theories*, which parsimoniously predict both aspects of the future (from past observations) and the domain in which these predictions are accurate. Specifically, we propose a novel generalized-mean-loss to encourage each theory to specialize in its comparatively advantageous domain, and a differentiable description length objective to downweight bad data and “snap” learned theories into simple symbolic formulas. Theories are stored in a “theory hub”, which continuously unifies learned theories and can propose theories when encountering new environments. We test our implementation, the “AI Physicist” learning agent, on a suite of increasingly complex physics environments. From unsupervised observation of trajectories through worlds involving random combinations of gravity, electromagnetism, harmonic motion and elastic bounces, our agent typically learns faster and produces mean-squared prediction errors about a billion times smaller than a standard feedforward neural net of comparable complexity, typically recovering integer and rational theory parameters exactly. Our agent successfully identifies domains with different laws of motion also for a nonlinear chaotic double pendulum in a piecewise constant force field.

I. INTRODUCTION

The ability to predict, analyze and parsimoniously model observations is not only central to the scientific endeavor, but also a goal of unsupervised machine learning, which is a key frontier in artificial intelligence (AI) research [1]. Despite impressive recent progress with artificial neural nets, they still get frequently outmatched by human researchers at such modeling, suffering from two drawbacks:

1. Different parts of the data are often generated by different mechanisms in different contexts. A big model that tries to fit all the data in one environment may therefore underperform in a new environment where some mechanisms are replaced by new ones, being inflexible and inefficient at combinatorial generalization [2].
2. Big models are generally hard to interpret, and may not reveal succinct and universal knowledge such as Newton’s law of gravitation that explains only some aspects of the data. The pursuit of “intelligible intelligence” in place of inscrutable black-box neural nets is important and timely, given the growing interest in AI interpretability from AI users and policymakers, especially for AI components involved in decisions and infrastructure where trust is important [3–6].

To address these challenges, we will borrow from physics the core idea of a *theory*, which parsimoniously predicts both aspects of the future (from past observations) and also the domain in which these predictions

Strategy	Definition
Divide-and-conquer	Learn multiple theories each of which specializes to fit <i>part</i> of the data very well
Occam’s Razor	Avoid overfitting by minimizing description length, which can include replacing fitted constants by simple integers or fractions.
Unification	Try unifying learned theories by introducing parameters
Lifelong Learning	Remember learned solutions and try them on future problems

TABLE I: AI Physicist strategies tested.

are accurate. This suggests an alternative to the standard machine-learning paradigm of fitting a single big model to all the data: instead, learning small theories one by one, and gradually accumulating and organizing them. This paradigm suggests the four specific approaches summarized in Table I, which we combine into a simple “AI Physicist” learning agent: To find individual theories from complex observations, we use the divide-and-conquer strategy with multiple theories and a novel generalized-mean loss that encourages each theory to specialize in its own domain by giving larger gradients for better-performing theories. To find simple theories that avoid overfitting and generalize well, we use the strategy known as Occam’s Razor, favoring simple theories that explain a lot, using a computationally efficient approximation of the minimum-description-length (MDL) formalism. To unify similar theories found in different environments, we use the description length for clustering and then learn a “master theory” for each class of theories. To accelerate future learning, we use a life-long-learning strategy where learned theories are stored

in a theory hub for future use.

Our approach complements other work on automatic program learning, such as neural program synthesis/induction [7–12] and symbolic program induction [13–17] and builds on prior machine-learning work on divide-and-conquer [18–21], network simplification [21–26] and continuous learning [27–30]. It is often said that babies are born scientists, and there is arguably evidence for use of all of these four strategies during childhood development as well [12].

The rest of this paper is organized as follows. In Section II, we introduce the architecture of our “AI Physicist” learning agent, and the algorithms implementing the four strategies. We present the results of our numerical experiments using a suite of physics environment benchmarks in Section III, and discuss our conclusions in Section IV, delegating supplementary technical details to a series of appendices.

II. METHODS

Unsupervised learning of regularities in time series can be viewed as a supervised learning problem of predicting the future from the past. This paper focuses on the task of predicting the next state vector $\mathbf{y}_t \in \mathbb{R}^d$ in a sequence from the concatenation $\mathbf{x}_t = (\mathbf{y}_{t-T}, \dots, \mathbf{y}_{t-1})$ of the last T vectors. However, our AI Physicist formalism applies more generally to learning any function $\mathbb{R}^M \mapsto \mathbb{R}^N$ from examples. In the following we first define *theory*, then introduce a unified AI Physicist architecture implementing the four aforementioned strategies.

A. Definition of Theory

A theory \mathcal{T} is a 2-tuple (\mathbf{f}, c) , where \mathbf{f} is a prediction function that predicts \mathbf{y}_t when \mathbf{x}_t is within the theory’s domain, and c is a domain sub-classifier which takes \mathbf{x}_t as input and outputs a logit of whether \mathbf{x}_t is inside this domain. When multiple theories are present, the sub-classifier c ’s outputs are concatenated and fed into a softmax function, producing probabilities for which theory is applicable. Both \mathbf{f} and c can be implemented by a neural net or symbolic formula, and can be set to learnable during training and fixed during prediction/validation.

This definition draws inspirations from physics theories (conditional statements), such as “a ball not touching anything (*condition*) with vertical velocity and height (v_0, h_0) will a time t later have $\mathbf{y} \equiv (v, h) = (v_0 - gt, h_0 + v_0t - gt^2/2)$ (*prediction function*)”. For our AI Physicist, theories constitute its “atoms” of learning, as well as the building blocks for higher-level manipulations.

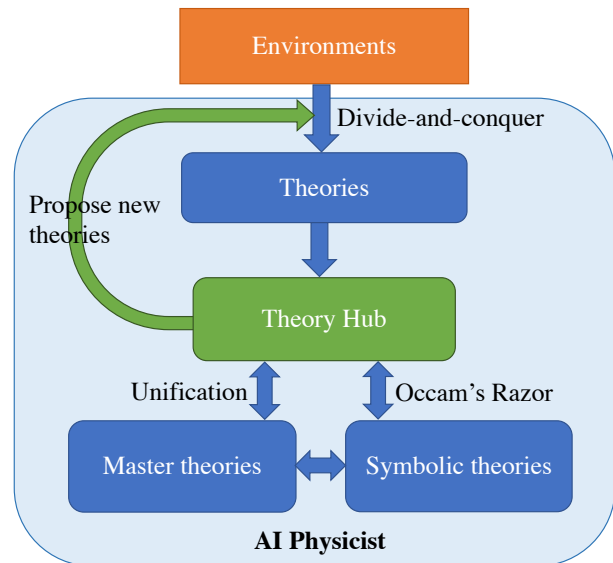


FIG. 1: AI Physicist Architecture

B. AI Physicist Architecture Overview

Figure 1 illustrates the architecture of the AI Physicist learning agent. At the center is a theory hub which stores the learned and organized theories. When encountering a new environment, the agent first inspects the hub and proposes old theories that help account for parts of the data as well as randomly initialized new theories for the rest of the data. All these theories are trained via our divide-and-conquer strategy, first jointly with our generalized-mean loss then separately to fine-tune each theory in its domain (section II C). Successful theories along with the corresponding data are added to the theory hub.

The theory hub has two organizing strategies: (1) Applying Occam’s Razor, it snaps the learned theories, in the form of neural nets, into simpler symbolic formulas (section II D). (2) Applying unification, it clusters and unifies the symbolic theories into master theories (section II E). The symbolic and master theories can be added back into the theory hub, improving theory proposals for new environments. The detailed AI Physicist algorithm is presented in a series of appendices.

C. Divide-and-Conquer

Conventionally, a function \mathbf{f} mapping $\mathbf{x}_t \mapsto \mathbf{y}_t$ is learned by parameterizing \mathbf{f} by some parameter vector $\boldsymbol{\theta}$ that is adjusted to minimize a loss (empirical risk)

$$\mathcal{L} \equiv \sum_t \ell[\mathbf{f}(\mathbf{x}_t), \mathbf{y}_t], \quad (1)$$

where ℓ is some non-negative distance function quantifying how far each prediction is from the target, typically satisfying $\ell(\mathbf{y}, \mathbf{y}) = 0$. In contrast, a physicist observing an unfamiliar environment does typically *not* try to predict everything with one model, instead starting with an easier question: is there any part or aspect of the world that can be described? For example, when Galileo famously tried to model the motion of swinging lamps in the Pisa cathedral, he completely ignored everything else, and made no attempts to simultaneously predict the behavior of sound waves, light rays, weather, or subatomic particles. In this spirit, we allow multiple competing theories $\mathcal{T} = \{\mathcal{T}_i\} = \{(\mathbf{f}_i, c_i)\}$, $i = 1, 2, \dots, M$, to specialize in different domains, with our proposed generalized-mean loss

$$\mathcal{L}_\gamma \equiv \sum_t \left(\frac{1}{M} \sum_{i=1}^M \ell[\mathbf{f}_i(\mathbf{x}_t), \mathbf{y}_t]^\gamma \right)^{1/\gamma} \quad (2)$$

When $\gamma < 0$, the loss \mathcal{L}_γ will be dominated by whichever prediction function \mathbf{f}_i fits each data point best. This dominance is controlled by γ , with $\mathcal{L}_\gamma \rightarrow \min_i \ell[\mathbf{f}_i(\mathbf{x}_t), \mathbf{y}_t]$ in the limit where $\gamma \rightarrow -\infty$. This means that the best way to minimize \mathcal{L}_γ is for each \mathbf{f}_i to specialize by further improving its accuracy for the data points where it already outperforms the other theories. The following Theorem 1 formalizes the above intuition, stating that under mild conditions for the loss function $\ell(\cdot, \cdot)$, the generalized-mean loss gives larger gradient w.r.t. the error $|\hat{\mathbf{y}}_t - \mathbf{y}_t|$ for theories that perform better, so that a gradient-descent loss minimization encourages specialization.

Theorem 1 *Let $\hat{\mathbf{y}}_t^{(i)} \equiv \mathbf{f}_i(\mathbf{x}_t)$ denote the prediction of the target \mathbf{y}_t by the function \mathbf{f}_i , $i = 1, 2, \dots, M$. Suppose that $\gamma < 0$ and $\ell(\hat{\mathbf{y}}_t, \mathbf{y}_t) = \ell(|\hat{\mathbf{y}}_t - \mathbf{y}_t|)$ for a monotonically increasing differentiable function $\ell(u)$ that vanishes on $[0, u_0]$ for some $u_0 \geq 0$, with $\ell(u)^\gamma$ strictly convex for $u > u_0$. Then if $0 < \ell(\hat{\mathbf{y}}_t^{(i)}, \mathbf{y}_t) < \ell(\hat{\mathbf{y}}_t^{(j)}, \mathbf{y}_t)$, we have*

$$\left| \frac{\partial \mathcal{L}_\gamma}{\partial u_t^{(i)}} \right| > \left| \frac{\partial \mathcal{L}_\gamma}{\partial u_t^{(j)}} \right|, \quad (3)$$

where $u_t^{(i)} \equiv |\hat{\mathbf{y}}_t^{(i)} - \mathbf{y}_t|$.

Appendix F gives the proof, and also shows that this theorem applies to mean-squared-error (MSE) loss $\ell(u) = u^2$, mean-absolute-error loss $\ell(u) = |u|$, Huber loss and our description-length loss from the next section.

We find empirically that the simple choice $\gamma = -1$ works quite well, striking a good balance between encouraging specialization for the best theory and also giving some gradient for theories that currently perform slightly worse. We term this choice \mathcal{L}_{-1} the ‘‘harmonic loss’’, because it corresponds to the harmonic mean of the losses for the different theories. Based on the harmonic loss,

we propose an unsupervised differentiable divide-and-conquer (DDAC) algorithm (Alg. 2 in Appendix B) that simultaneously learns prediction functions $\{\mathbf{f}_i\}$ and corresponding domain classifiers $\{c_i\}$ from observations.

D. Occam’s Razor

The principle of Occam’s Razor, that simpler explanations are better, is quite popular among physicists. This preference for parsimony helped dispense with phlogiston, aether and other superfluous concepts.

Our method therefore incorporates the minimum-description-length (MDL) formalism [22, 25], which provides an elegant mathematical implementation of Occam’s Razor. The description length (DL) of a dataset D is defined as the number of bits required to describe it. For example, if regularities are discovered that enable data compression, then the corresponding description length is defined as the number of bits of the program that produces D as its output (including both the code bits and the compressed data bits). In our context of predicting a time series, this means that the description length is the number of bits required to describe the theories used plus the number of bits required to store all prediction errors. Finding the optimal data compression and hence computing the MDL is a famous hard problem that involves searching an exponentially large space, but any discovery reducing the description length is a step in the right direction, and provably avoids the overfitting problem that plagues many alternative machine-learning strategies [22, 25]. Commonly used neural nets often provide poor data compression, leaving ample room for improvement [31].

The end-goal of the AI Physicist is to discover theories \mathcal{T} minimizing the total description length, given by

$$\text{DL}(\mathcal{T}, D) = \text{DL}(\mathcal{T}) + \sum_t \text{DL}(\mathbf{u}_t), \quad (4)$$

where $\mathbf{u}_t = \hat{\mathbf{y}}_t - \mathbf{y}_t$ is the prediction error at time step t . By discovering simple theories that can each account for parts of the data very well, the AI Physicist strives to make both $\text{DL}(\mathcal{T})$ and $\sum_t \text{DL}(\mathbf{u}_t)$ small.

Physics has enjoyed great success in its pursuit of simpler theories using rather vague definitions of simplicity. In the this spirit, we choose to compute the description length DL not exactly, but using an approximate heuristic that is numerically efficient, and significantly simpler than more precise versions such as [32]. We compute the DL of both theories \mathcal{T} and prediction errors \mathbf{u}_t as the sum of the DL of all numbers that specify them, using the following conventions for the DL of integers, rational numbers and real numbers.

The number of binary digits required to specify a natural number $n = 1, 2, 3, \dots$ is approximately $\log_2 n$, so we define $\text{DL}(n) \equiv \log_2 n$ for natural numbers. For an integer

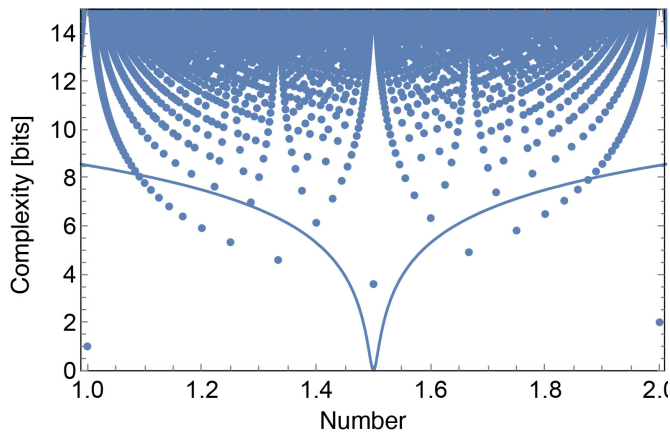


FIG. 2: The description length $DL(q)$ is shown for the rational numbers $q \in [1, 2]$. Occam's Razor favors dots further down. Our MDL rational approximation of a real number u is the lowest point after adding a suitably shifted and scaled \log_+ function (solid curve, here centered on $r = 1.5000017$).

m , we define

$$DL(m) \equiv \log_2(1 + |m|). \quad (5)$$

For a rational number $q = m/n$, the description length is the sum of that for its integer numerator and (natural number) denominator, as illustrated in Figure 2:

$$DL\left(\frac{m}{n}\right) = \log_2[(1 + |m|)n]. \quad (6)$$

For a real number r and a numerical precision floor ϵ , we define

$$DL(r) = \log_+\left(\frac{r}{\epsilon}\right), \quad (7)$$

where the function

$$\log_+(x) \equiv \frac{1}{2} \log_2(1 + x^2) \quad (8)$$

is plotted in Figure 2. Since $\log_+(x) \approx \log_2 x$ for $x \gg 1$, $DL(r)$ is approximately the description length of the integer closest to r/ϵ . Since $\log_+(x) \propto x^2$ for $x \ll 1$, $DL(r)$ simplifies to a quadratic (mean-squared-error) loss function below the numerical precision, which will prove useful below.¹

Note that as long as all prediction absolute errors $|u_i| \gg \epsilon$ for some dataset, minimizing the total description length $\sum_i DL(u_i)$ instead of the MSE $\sum_i u_i^2$ corresponds to minimizing the geometric mean instead of the arithmetic mean of the squared errors, which encourages focusing

more on improving already well-fit points. $\sum_i DL(u_i)$ drops by 1 bit whenever one prediction error is halved, which is can typically be achieved by fine-tuning the fit for many valid data points that are already well predicted while increasing DL for bad or extraneous points at most marginally.

For numerical efficiency, our AI Physicist minimizes the description length of equation (4) in two steps: 1) All model parameters are set to trainable real numbers, and the DDAC algorithm is applied to minimize the harmonic loss \mathcal{L}_{-1} with $\ell(\mathbf{u}) \equiv \sum_i DL(u_i)$ using equation (7) and the annealing procedure for the precision floor described in Appendix B. 2) Some model parameters are replaced by rational numbers as described below, followed by re-optimization of the other parameters. The idea behind the second step is that if a physics experiment or neural net training produces a parameter $p = 1.4999917$, it would be natural to interpret this as a hint, and to check if $p = 3/2$ gives an equally acceptable fit to the data, reducing total DL. We implement step 2 using continued fraction expansion as described in Appendix C and illustrated in Figure 3.

E. Unification

Physicists aspire not only to find simple theories that explain aspects of the world accurately, but also to discover underlying similarities between theories and *unify* them. For example, when James Clerk Maxwell corrected and unified four key formulas describing electricity and magnetism into his eponymous equations ($d\mathbf{F} = 0$, $d\star\mathbf{F} = \mathbf{J}$ in differential form notation), he revealed the nature of light and enabled the era of wireless communication.

Here we make a humble attempt to automate part of this process. The goal of the unification is to output a master theory $\mathcal{T} = \{(\mathbf{f}_{\mathbf{p}}, \cdot)\}$, such that varying the parameter vector $\mathbf{p} \in \mathbb{R}^n$ can generate a continuum of theories $(\mathbf{f}_{\mathbf{p}}, \cdot)$ including previously discovered ones. For example, Newton's law of gravitation can be viewed as a master theory unifying the gravitational force formulas around different planets by introducing a parameter p corresponding to planet mass. Einstein's special relativity can be viewed as a master theory unifying the approximate formulas for $v \ll c$ and $v \approx c$ motion.

We perform unification by first computing the description length $dl^{(i)}$ of the prediction function \mathbf{f}_i (in symbolic form) for each theory i and performing clustering on $\{dl^{(i)}\}$. Unification is then achieved by discovering similarities and variations between the symbolic formulas in each cluster, retaining the similar patterns, and introducing parameters in place of the parameters that vary as detailed in Appendix D.

¹ Natural alternative definitions of $\log_+(x)$ include $\log_2(1 + |x|)$, $\log_2 \max(1, |x|)$, $(\ln 2)^{-1} \sinh^{-1} |x|$ and $(2 \ln 2)^{-1} \sinh^{-1}(x^2)$. Unless otherwise specified, we choose $\epsilon = 2^{-32}$ in our experiments.

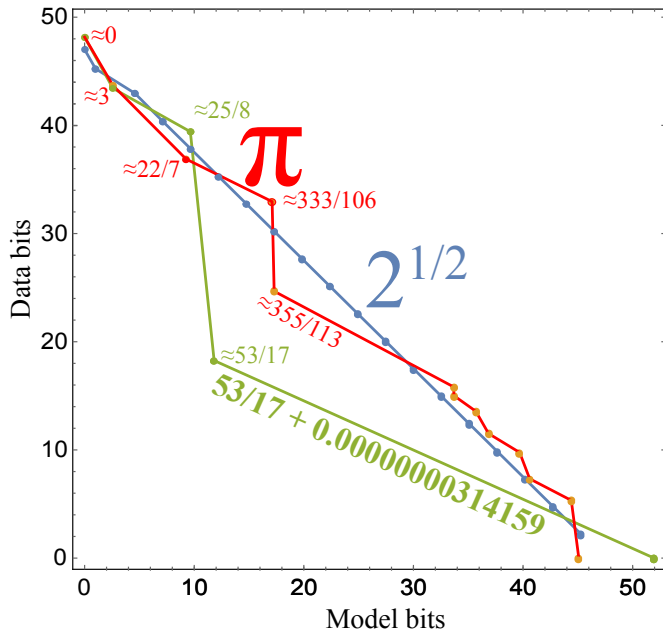


FIG. 3: Illustration of our minimum-description-length (MDL) analysis of the parameter vector $\mathbf{p} = \{\pi, \sqrt{2}, 3.43180632382353\}$. We approximate each real number r as a fraction a_k/b_k using the first k terms of its continued fraction expansion, and for each integer $k = 1, \dots$, we plot the number of “data bits” required to encode the prediction error $r - a_k/b_k$ to 14 decimal places versus the number of “model bits” required to encode the rational approximation a_k/b_k , as described in the text. We then select the point with smallest bit sum (furthest down/left from the diagonal) as our first approximation candidate to test. Generic irrational numbers are incompressible; the total description length (model bits+data bits) is roughly independent of k as is seen for π and $\sqrt{2}$, corresponding to a line of slope -1 around which there are small random fluctuations. In contrast, the green/light grey curve (bottom) is for a parameter that is anomalously close to a rational number, and the curve reveals this by the approximation $53/17$ reducing the total description length (model+data bits) by about 16 bits.

F. Lifelong Learning

Isaac Newton once said “If I have seen further it is by standing on the shoulders of giants”, emphasizing the utility of building on past discoveries. At a more basic level, our past experiences enable us humans to model new environments much faster than if we had to re-acquire all our knowledge from scratch. We therefore embed a lifelong-learning strategy into the architecture of the AI Physicist. As shown in Fig. 1 and Alg. 1, the theory hub stores successfully learned theories, organizes them with our Occam’s-Razor and unification algorithms (reminiscent of what humans do while dreaming and reflecting), and when encountering new environments, uses

its accumulated knowledge to propose new theories that can explain parts of the data. This both ensures that past experiences are not forgotten and enables faster learning in novel environments. The detailed algorithms for proposing and adding theories are in Appendix E.

III. RESULTS OF NUMERICAL EXPERIMENTS

A. Physics Environments

We test our algorithms on two suites of benchmarks, each with increasing complexity. In all cases, the goal is to predict the two-dimensional motion as accurately as possible. One suite involves chaotic and highly nonlinear motion of a charged double pendulum in two adjacent electric fields. The other suite involves balls affected by gravity, electromagnetic fields, springs and bounce-boundaries, as exemplified in Figure 4. Within each spatial region, the force corresponds to a potential energy function $V \propto (ax + by + c)^n$ for some constants a, b, c , where $n = 0$ (no force), $n = 1$ (uniform electric or gravitational field), $n = 2$ (spring obeying Hooke’s law) or $n = \infty$ (ideal elastic bounce), and optionally involves also a uniform magnetic field. The environments are summarized in Table II.

B. Numerical Results

In the mystery world example of Figure 4, after the DDAC algorithm 2) taking the sequence of coordinates as the only input, we see that the AI Physicist has learned to simultaneously predict the future position of the ball from the previous two, and classify without external supervision the observed inputs into four big physics domains. The predictions are seen to be more accurate deep inside the domains (tiny dots) than near boundaries (larger dots) where transitions and bounces create small domains with laws of motion that are harder to infer because of complexity and limited data. Because these small domains can be automatically inferred and eliminated once the large ones are known as described in Appendix G, all accuracy benchmarks quoted below refer to points in the large domains only.

After DDAC, the AI Physicist performs MDL-Occam’s-razor (Alg. 3) on the learned theories. As an example, it discovers that the motion deep inside the lower-left quadrant obeys the difference equation parameterized by a learned 3-layer neural net, which after the first collapse-layer transformation simplifies to

$$\hat{\mathbf{y}}_t = \begin{pmatrix} -0.99999994 & 0.00000006 & 1.99999990 & -0.00000012 \\ -0.00000004 & -1.00000000 & 0.00000004 & 2.00000000 \end{pmatrix} \mathbf{x}_t + \begin{pmatrix} 0.01088213 \\ -0.00776199 \end{pmatrix}, \quad (9)$$

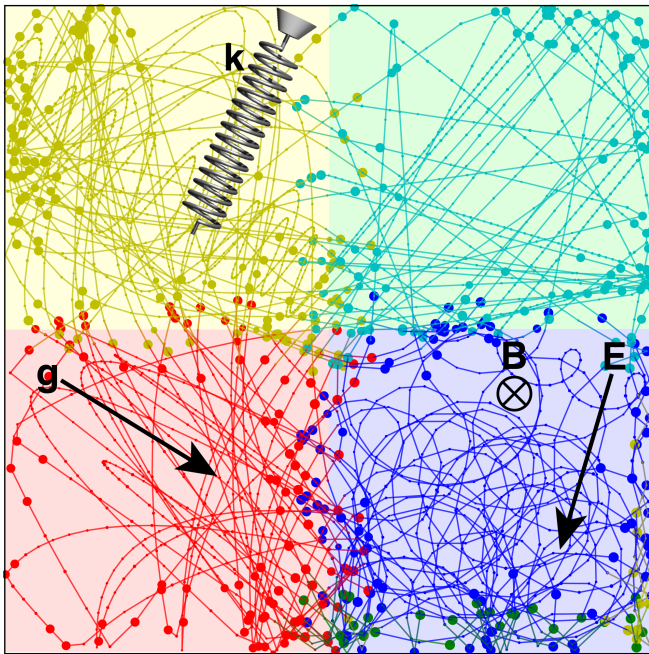


FIG. 4: In this sample mystery world, a ball moves through a harmonic potential (upper left quadrant), a gravitational field (lower left) and an electromagnetic field (lower right quadrant) and bounces elastically from four walls. The only input to the AI Physicist is the sequence of dots (ball positions); the challenge is to learn all boundaries and laws of motion (predicting each position from the previous two). The color of each dot represents the domain into which it is classified by \mathbf{c} , and its area represents the description length of the error with which its position is predicted ($\epsilon = 10^{-6}$) after the DDAC (differentiable divide-and-conquer) algorithm; the AI Physicist tries to minimize the total area of all dots.

with $DL(\mathbf{f}) = 212.7$ and $DL(\mathbf{u}_t) = 2524.1$. The snapping stage thereafter simplifies to

$$\hat{\mathbf{y}}_t = \begin{pmatrix} -1 & 0 & 2 & 0 \\ 0 & -1 & 0 & 2 \end{pmatrix} \mathbf{x}_t + \begin{pmatrix} 0.010882 \\ -0.007762 \end{pmatrix}. \quad (10)$$

which has lower description length in both model bits ($DL(\mathbf{f}) = 55.6$) and data bits ($DL(\mathbf{u}_t) = 2519.6$) and gets transformed to the symbolic expressions

$$\begin{aligned} \hat{x}_{t+2} &= 2x_{t+1} - x_t + 0.010882, \\ \hat{y}_{t+2} &= 2y_{t+1} - y_t - 0.007762, \end{aligned} \quad (11)$$

where we have written the 2D position vector $\mathbf{y} = (x, y)$ for brevity. During unification (Alg. D), the AI Physicist discovers multiple clusters of theories based on the DL of each theory, where one cluster has DL ranging between 48.86 and 55.63, which it unifies into a master theory \mathbf{f}_q with

$$\begin{aligned} \hat{x}_{t+2} &= 2x_{t+1} - x_t + q_1, \\ \hat{y}_{t+2} &= 2y_{t+1} - y_t + q_2, \end{aligned} \quad (12)$$

effectively discovering a “gravity” master theory out of the different types of environments it encounters. If so

desired, the difference equations (12) can be automatically generalized to the more familiar-looking differential equations

$$\begin{aligned} \ddot{x} &= g_x, \\ \ddot{y} &= g_y, \end{aligned}$$

where $g_i \equiv q_i(\Delta t)^2$, and both the Harmonic Oscillator Equation and Lorentz Force Law of electromagnetism can be analogously auto-inferred from other master theories learned.

Many mystery domains in our test suite involve laws of motion whose parameters include both rational and irrational numbers. To count a domain as “solved” below, we use the very stringent requirement that any rational numbers (including integers) must be discovered *exactly*, while irrational numbers must be recovered with accuracy 10^{-4} .

We apply our AI Physicist to 40 mystery worlds in sequence (Appendix H). After this training, we apply it to a suite of 40 additional worlds to test how it learns different numbers of examples. The results are shown tables III and IV, and Table II summarizes these results using the median over worlds. For comparison, we also show results for two simpler agents with similar parameter count: a “baseline” agent consisting of a three-layer feedforward MSE-minimizing leakyReLU network and a “newborn” AI Physicist that has not seen any past examples and therefore cannot benefit from the lifelong-learning strategy.

We see that the newborn agent outperforms baseline on all the tabulated measures, and that the AI Physicist does still better. Using all data, the Newborn agent and AI Physicist is able to predict with mean-squared prediction error below 10^{-13} , more than nine orders of magnitude below baseline. Moreover, the Newborn and AI Physicist agents are able to simultaneously learn the domain classifiers with essentially perfect accuracy, without external supervision. Both agents are able to solve above 90% of all the 40 mystery worlds according to our stringent criteria.

The main advantage of the AI Physicist over the Newborn agent is seen to be its learning speed, attaining given accuracy levels faster, especially during the early stage of learning. Remarkably, for the subsequent 40 worlds, the AI Physicist reaches 0.01 MSE within 35 epochs using as little as 1% of the data, performing almost as well as with 50% of the data much getter than the Newborn agent. This illustrates that the lifelong learning strategy enables the AI Physicist to learn much faster in novel environments with less data. This is much like an experienced scientist can solve new problems way faster than a beginner by building on prior knowledge about similar problems.

Our double-pendulum mysteries (Appendix H2) are more challenging for all the agents, because the motion is

Benchmark	Baseline	Newborn	AI Physicist
\log_{10} mean-squared error	-3.89	-13.95	-13.88
Classification accuracy	67.56%	100.00%	100.00%
Fraction of worlds solved	0.00%	90.00%	92.50%
Description length for \mathbf{f}	11,338.7	198.9	198.9
Epochs until 0.01 MSE	95	83	15
Epochs until 0.0001 MSE	6925	330	45
Epochs until 10^{-6} MSE	∞	5403	3895
Epochs until 10^{-8} MSE	∞	6590	5100
\log_{10} MSE error			
using 100% of data	-3.78	-13.89	-13.89
using 50% of data	-3.84	-13.76	-13.81
using 10% of data	-3.16	-7.38	-10.54
using 5% of data	-3.06	-6.06	-6.20
using 1% of data	-2.46	-3.69	-3.95
Epochs until 0.01 MSE			
using 100% of data	95	80	15
using 50% of data	190	152.5	30
using 10% of data	195	162.5	30
using 5% of data	205	165	30
using 1% of data	397.5	235	35

TABLE II: Summary of numerical results, taking the median over 40 mystery environments from Table III (top part) and on 40 novel environments with varying fraction of random examples (bottom parts), where each world is run with 10 random initialization and taking the best performance. Accuracies refer to big regions only.

more nonlinear and indeed chaotic. Although none of our double-pendulum mysteries get exactly solved according to our very stringent above-mentioned criterion, Figure 7 illustrates that the Newborn agent does a good job: it discovers the two domains and classifies points into them with an accuracy of 96.5%. Overall, the Newborn have a median best accuracy of 91.0% compared with the baseline of 76.9%. The MSE prediction error is comparable to the baseline performance ($\sim 4 \times 10^{-4}$) in the median, since both architectures have similar large capacity. We analyze this challenge and opportunities for improvement below.

IV. CONCLUSIONS

We have presented a simple “AI Physicist” unsupervised learning agent centered around the learning and manipulation of theories, which parsimoniously predict both aspects of the future (from past observations) and the domain in which these predictions are accurate. Testing it on a suite of mystery worlds involving random combinations of gravity, electromagnetism, harmonic motion and elastic bounces, we found that its divide-and-conquer and Occam’s Razor strategies effectively identified domains with different laws of motion and reduced the mean-squared prediction error billionfold, typically recovering integer and rational theory parameters exactly. These two strategies both encouraged prediction functions to

specialize: the former on the domains they handled best, and the latter on the data points within their domain that they handled best. Adding the lifelong-learning strategy greatly accelerated learning in novel environments.

Our work suggests many opportunities for improvement of the implementation. The more modest success in the double-pendulum experiments illustrated the value of learned theories being *simple*: if they are highly complex, they are less likely to unify or generalize to future environments, and the correspondingly complex baseline model will have enough expressive power to approximate the motion in all domains at once. It will be valuable to improve techniques for simplifying complex learned neural nets (reducing their total description length from equation (4)), for example by using Monte-Carlo-Markov-Chain-based and genetic techniques [33], reinforcement learning [34, 35] and analytic regression [36] literature to simplify and shrink the model architecture. It will also be interesting to generalize our implementation to simplify not only the prediction functions, but also the classifiers, for example to find sharp domain boundaries composed of hyperplanes or other simple surfaces. These and other improvements to the algorithms that implement our AI Physicist paradigm could enable future unsupervised learning agents to learn simpler and more accurate models faster from fewer examples.

Acknowledgements: This work was supported by the The Casey and Family Foundation, the Foundational Questions Institute and the Rothberg Family Fund for Cognitive Science. We thank Isaac Chuang, John Peurifoy and Marin Soljačić for helpful discussions and suggestions, and the Center for Brains, Minds, and Machines (CBMM) for hospitality.

Appendix A: AI Physicist Algorithm

The detailed AI Physicist algorithm is presented Algorithm 1, with links to each of the individual sub-algorithms.

Algorithm 1 AI Physicist: Overall algorithm

Given observations $D = \{(\mathbf{x}_t, \mathbf{y}_t)\}$ from new environment:

- 1: $\mathcal{T}_{M_0} \leftarrow \mathbf{Hub.propose-theories}(D, M_0)$ (Alg. 6)
- 2: $\mathcal{T} \leftarrow \mathbf{divide-and-conquer}(D, \mathcal{T}_{M_0})$ (Alg. 2)
- 3: $\mathbf{Hub.add-theories}(\mathcal{T}, D)$ (Alg. 5)

Organizing theory hub:

- $\mathcal{T} \leftarrow \mathbf{Hub.Occam's-Razor-with-MDL}(\mathcal{T}, D)$ (Alg. 3)
 - $\mathcal{T} \leftarrow \mathbf{Hub.unify}(\mathcal{T})$ (Alg. 4)
-

Appendix B: The Differentiable Divide-and-Conquer (DDAC) Algorithm

Here we elaborate on our proposed differentiable divide-and-conquer (DDAC) algorithm with generalized-mean loss (Eq. (2)). This loss with $\gamma < 0$ works with a broad range of distance functions ℓ satisfying Theorem 1. Since the goal of our AI Physicist is to minimize the overall description length (DL) from equation (4), we choose ℓ to be the DL loss function of equation (7) together with $\gamma = -1$ (harmonic loss), which works quite well in practice.

Algorithm 2 describes our divide-and-conquer implementation, which consists of two stages. In the first stage (steps 2-6), it applies the subroutine $\mathbf{HarmonicTrain}(\mathcal{T}, \ell_{DL, \epsilon}, D)$ to train the theories \mathcal{T} a few times with the precision floor ϵ gradually lowered according to the following annealing schedule. We set the initial precision floor ϵ to be quite large so that ℓ initially approximates an MSE loss function. After each successive iteration, we reset ϵ to the median prediction error.

The DL loss function from equation (7) is theoretically desirable but tricky to train, both because it is non-convex and because it is quite flat and uninformative far from its minimum. Our annealing schedule helps overcome both problems: initially when ϵ is large, it approximates MSE-loss which is convex and guides the training to a good approximate minimum, which further training accurately pinpoints as ϵ is reduced.

The subroutine $\mathbf{HarmonicTrain}$ forms the core of the algorithm. It uses the harmonic mean of the DL-loss of multiple prediction functions $\mathbf{f}_\theta = (\mathbf{f}_1, \dots, \mathbf{f}_M)$ (*i.e.*, equation (2) with $\gamma = -1$ and $\ell = \text{DL}$) to simultaneously train these functions, encouraging them to each specialize in the domains where they predict best (as proven by Theorem 1), and simultaneously trains the domain classifier $\mathbf{c}_\phi = (c_1, \dots, c_M)$ using each example's best-performing

Algorithm 2 AI Physicist: Differentiable Divide-and-Conquer with Harmonic Loss

Require Dataset $D = \{(\mathbf{x}_t, \mathbf{y}_t)\}$

Require M : number of initial total theories for training

Require $\mathcal{T}_{M_0} = \{(\mathbf{f}_i, c_i)\}, i = 1, \dots, M_0, 0 \leq M_0 \leq M$: theories proposed from theory hub

Require K : number of gradient iterations

Require β_f, β_c : learning rates

Require ϵ_0 : initial precision floor

- 1: Randomly initialize $M - M_0$ theories $\mathcal{T}_i, i = M_0 + 1, \dots, M$. Denote $\mathcal{T} = (\mathcal{T}_1, \dots, \mathcal{T}_M)$, $\mathbf{f}_\theta = (f_1, \dots, f_M)$ with learnable parameters θ ; $\mathbf{c}_\phi = (c_1, \dots, c_M)$ with learnable parameters ϕ .

// Harmonic training with DL loss:

2: $\mathcal{T} \leftarrow \mathbf{HarmonicTrain}(\mathcal{T}, \ell_{DL, \epsilon_0}, D)$

3: $\epsilon \leftarrow \epsilon_0$

4: **for** k in $\{1, 2, 3, 4\}$ **do**:

5: $\mathcal{T} \leftarrow \mathbf{HarmonicTrain}(\mathcal{T}, \ell_{DL, \epsilon}, D)$

6: $\epsilon \leftarrow \text{set_epsilon}(D)$ // median prediction error

7: **end for**

// Fine-tune each theory in its domain:

8: **for** i in $\{1, \dots, M\}$ **do**:

9: $D^{(i)} \leftarrow \{(\mathbf{x}_t, \mathbf{y}_t) \mid \arg \max_j \{c_j(\mathbf{x}_t)\} = i\}$

10: $\mathbf{f}_i \leftarrow \text{Minimize}_{\mathbf{f}_i} \sum_{(\mathbf{x}_t, \mathbf{y}_t) \in D^{(i)}} \ell_{DL, \epsilon}[\mathbf{f}_i(\mathbf{x}_t), \mathbf{y}_t]$

11: **end for**

12: **return** \mathcal{T}

subroutine $\mathbf{HarmonicTrain}(\mathcal{T}, \ell, D)$:

s1: **for** k in $\{1, \dots, K\}$ **do**:

 // Gradient descent on \mathbf{f}_θ with harmonic loss:

s2: $\mathcal{L}_f \leftarrow \sum_{(\mathbf{x}_t, \mathbf{y}_t) \in D} M / (\sum_{i=1}^M \frac{1}{\ell[\mathbf{f}_i(\mathbf{x}_t), \mathbf{y}_t]})$

s3: $\theta \leftarrow \theta - \beta_f \nabla_{\theta} \mathcal{L}_f$

 // Gradient descent on \mathbf{c}_ϕ with the best performing theory index as target:

s4: $b_i \leftarrow \arg \min_i \{\ell[\mathbf{f}_i(\mathbf{x}_t), \mathbf{y}_t]\}, \forall t$

s5: $\mathcal{L}_c \leftarrow \sum_{(\mathbf{x}_t, \cdot) \in D} \text{CrossEntropy}[\text{softmax}(\mathbf{c}_\phi(\mathbf{x}_t)), b_i]$

s6: $\phi \leftarrow \phi - \beta_c \nabla_{\phi} \mathcal{L}_c$

s7: **end for**

s8: $\mathcal{T} \leftarrow \text{AddTheories}(\mathcal{T}, D)$ //Optional

s9: $\mathcal{T} \leftarrow \text{DeleteTheories}(\mathcal{T}, D)$ //Optional

s10: **return** \mathcal{T}

prediction function as target, with categorical cross-entropy loss. After several rounds of $\mathbf{HarmonicTrain}$ with successively lower precision floors, each prediction function typically becomes good at predicting part of the dataset, and the domain classifier becomes good at predicting for each example which prediction function will predict best.

$\text{AddTheories}(\mathcal{T}, D)$ inspects each theory \mathcal{T}_i describing at least a large fraction (we use 30%) of the examples to see if a non-negligible proportion of examples (we use a threshold of 5%) of the examples inside its domain have error larger than a certain limit (we use 2×10^{-6}). If so, it uses those examples to initialize a new theory \mathcal{T}_{M+1} , and performs tentative training together with other theories using $\mathbf{HarmonicTrain}$ without steps s8 and s9. If the

resulting harmonic loss \mathcal{L}_γ is smaller than before adding the new theory, \mathcal{T}_{M+1} is accepted and retained, otherwise it is rejected and training reverts to the checkpoint before adding the theory. `DeleteTheories`(\mathcal{T}, D) deletes theories whose domain or best-predicted examples cover a negligible fraction of the examples (we use a delete threshold of 0.5%) .

In the second stage (steps 7-10), the domain classifier $\mathbf{c} = (c_1, c_2, \dots, c_M)$ is used to predict each theory’s domain, and fine-tunes each prediction function \mathbf{f}_i only on the examples classified as belonging to its domain. The reason that we assign examples to domains using our domain classifier rather than prediction accuracy is that the trained domains are likely to be simpler and more contiguous, thus generalizing better to unseen examples than, *e.g.*, the nearest neighbor algorithm.

We now we specify the hyperparameters used for Algorithm 1 in our experiments. We set M_0 , the number of theories proposed from theory hub, to be 2 for all experiments. We set the number of initial total theories for training to be $M = 4$ for mystery-world experiments and $M = 3$ for double pendulum experiments. We set the initial precision floor $\epsilon = 10$ and the number of gradient iterations $K = 10000$. We use the Adam [37] optimizer with default parameters for the optimization of both the prediction function and the domain classifier. We set the initial learning rate $\beta = 5 \times 10^{-3}$ for the prediction functions \mathbf{f}_θ and $\beta = 10^{-3}$ for the domain classifier \mathbf{c}_ϕ . We also use a learning rate scheduler that monitors the validation loss every 10 epochs, and divides the learning rate by 10 if the validation loss has failed to decrease after 40 epochs and stops training early if there is no decrease after 200 epochs — or if the entire MSE loss for all the theories in their respective domains drops below 10^{-12} .

To the main harmonic loss \mathcal{L}_γ , we add two regularization terms. One is L_1 loss whose strength increases quadratically from 0 to 10^{-8} (to 10^{-7} in the double-pendulum experiment) during the first 5000 epochs and remains constant thereafter. The second regularization term is a very small MSE loss of strength 10^{-7} , to encourage the theories to remain not too far away from the target outside their domain.

Appendix C: Occam’s Razor algorithm

Pushing on after the differentiable divide-and-conquer algorithm with harmonic loss that minimizes the $\sum_t \text{DL}(\mathbf{u}_t)$ term in Eq. (4), the AI Physicist then strives to minimize the $\text{DL}(\mathcal{T})$ term, which can be decomposed as $\text{DL}(\mathcal{T}) = \text{DL}(\mathbf{f}_\theta) + \text{DL}(\mathbf{c}_\phi)$, where $\mathbf{f}_\theta = (\mathbf{f}_1, \dots, \mathbf{f}_M)$ and $\mathbf{c}_\phi = (c_1, \dots, c_M)$. We focus on minimizing $\text{DL}(\mathbf{f}_\theta)$, since in different environments the prediction functions \mathbf{f}_i can often be reused, while the domains may differ. As mentioned, we define $\text{DL}(\mathbf{f}_\theta)$ simply as the sum of the

description lengths of the number parameterizing \mathbf{f}_θ :

$$\text{DL}(\mathbf{f}_\theta) = \sum_j \text{DL}(\theta_j). \quad (\text{C1})$$

This means that $\text{DL}(\mathbf{f}_\theta)$ can be significantly reduced if an irrational parameter is replaced by a simple rational number.

Algorithm 3 AI Physicist: Occam’s Razor with MDL

Require Dataset $D = \{(\mathbf{x}_t, \mathbf{y}_t)\}$
Require $\mathcal{T} = \{(\mathbf{f}_i, c_i)\}, i = 1, \dots, M$: theories trained after Alg. 2
Require ϵ : Precision floor for $\ell_{DL, \epsilon}$
1: **for** i in $\{1, \dots, M\}$ **do**:
2: $D^{(i)} \leftarrow \{(\mathbf{x}_t, \mathbf{y}_t) \mid \arg \max_j \{c_j(\mathbf{x}_t)\} = i\}$
3: $\mathbf{f}_i \leftarrow \text{MinimizeDL}(\text{collapseLayers}, \mathbf{f}_i, D^{(i)}, \epsilon)$
4: $\mathbf{f}_i \leftarrow \text{MinimizeDL}(\text{localSnap}, \mathbf{f}_i, D^{(i)}, \epsilon)$
5: $\mathbf{f}_i \leftarrow \text{MinimizeDL}(\text{integerSnap}, \mathbf{f}_i, D^{(i)}, \epsilon)$
6: $\mathbf{f}_i \leftarrow \text{MinimizeDL}(\text{rationalSnap}, \mathbf{f}_i, D^{(i)}, \epsilon)$
7: $\mathbf{f}_i \leftarrow \text{MinimizeDL}(\text{toSymbolic}, \mathbf{f}_i, D^{(i)}, \epsilon)$
8: **end for**
9: **return** \mathcal{T}

subroutine `MinimizeDL`(transformation, $\mathbf{f}_i, D^{(i)}, \epsilon$):
s1: **while** transformation.is_applicable(\mathbf{f}_i) **do**:
s2: $\text{dl}_0 \leftarrow \text{DL}(\mathbf{f}_i) + \sum_{(\mathbf{x}_t, \mathbf{y}_t) \in D^{(i)}} \ell_{DL, \epsilon}[\mathbf{f}_i(\mathbf{x}_t), \mathbf{y}_t]$
s3: $f_{\text{clone}} \leftarrow \mathbf{f}_i$ // clone \mathbf{f}_i in case transformation fails
s4: $\mathbf{f}_i \leftarrow \text{transformation}(\mathbf{f}_i)$
s5: $\mathbf{f}_i \leftarrow \text{Minimize}_{\mathbf{f}_i} \sum_{(\mathbf{x}_t, \mathbf{y}_t) \in D^{(i)}} \ell_{DL, \epsilon}[\mathbf{f}_i(\mathbf{x}_t), \mathbf{y}_t]$
s6: $\text{dl}_1 \leftarrow \text{DL}(\mathbf{f}_i) + \sum_{(\mathbf{x}_t, \mathbf{y}_t) \in D^{(i)}} \ell_{DL, \epsilon}[\mathbf{f}_i(\mathbf{x}_t), \mathbf{y}_t]$
s7: **if** $\text{dl}_1 > \text{dl}_0$ **return** f_{clone}
s8: **end while**
s9: **return** \mathbf{f}_i

If a physics experiment or neural net training produces a parameter $p = 1.999942$, it would be natural to interpret this as a hint, and to check if $p = 2$ gives an equally acceptable fit to the data. We formalize this by replacing any real-valued parameter p_i in our theory \mathcal{T} by its nearest integer if this reduces the total description length in equation (4), as detailed below. We start this search for integer candidates with the parameter that is closest to an integer, refitting with the other parameters after each successful “integer snap”.

What if we instead observe a parameter $p = 1.5000017$? Whereas generic real numbers have a closest integer, they lack a closest rational number. Moreover, as illustrated in Figure 2, we care not only about closeness (to avoid increasing the second term in equation (4)), but also about simplicity (to reduce the first term). To rapidly find the best “rational snap” candidates (dots in Figure 2 that lie both near p and far down), we perform a continued fraction expansion of p and use each series truncation as a rational candidate. We repeat this for all parameters in the theory \mathcal{T} , again accepting only those snaps that reduce the total description length. We again wish to try

the most promising snap candidates first; to rapidly identify promising candidates without having to recompute the second term in equation (4), we evaluate all truncations of all parameters as in Figure 3, comparing the description length of the rational approximation $q = m/n$ with the description length of the approximation error $|p - q|$. The most promising candidate minimizes their sum, *i.e.*, lies furthest down to the left of the diagonal in the figure. The figure illustrates how, given the parameter vector $\mathbf{p} = \{\pi, \sqrt{2}, 3.43180632382353\}$, the first snap to be attempted will replace the third parameter by $53/17$.

We propose Algorithm 3 to implement the above minimization of $\text{DL}(\mathbf{f}_\theta)$ without increasing $\sum_t \text{DL}(\mathbf{u}_t)$. For each theory $\mathcal{T}_i = (\mathbf{f}_i, c_i)$, we first extract the examples $D^{(i)}$ inside its domain, then perform a series of tentative transformations (simplifications) of the prediction function \mathbf{f}_i using the `MinimizeDL` subroutine. This subroutine takes \mathbf{f}_i , the transformation, and $D^{(i)}$ as inputs and repeatedly applies the transformation to \mathbf{f}_i . After each such transformation, it fine-tunes the fit of \mathbf{f}_i to $D^{(i)}$ using gradient descent. For determining whether to accept the transformation, Algorithm 3 presents the simplest 0-step patience implementation: if the description length $\text{dl} = \text{DL}(\mathbf{f}_i) + \sum_{(\mathbf{x}_t, \mathbf{y}_t) \in D^{(i)}} \ell_{\text{DL}, \epsilon}(\mathbf{f}_i(\mathbf{x}_t), \mathbf{y}_t)$ for theory i decreases, then apply the transformation again if possible, otherwise exit the loop. In general, to allow for temporary increase of DL during the transformations, a non-zero patience can be adopted: at each step, save the best performing model as the pivot model, and if DL does not decrease during n consecutive transformations inside `MinimizeDL`, exit the loop. In our implementation, we use a 4-step patience.

We now detail the five transformations used in Algorithm 3. The `collapseLayer` transformation finds all successive layers of a neural net where the lower layer has linear activation, and combines them into one. The `toSymbolic` transformation transforms \mathbf{f}_i from the form of a neural net into a symbolic expression (in our implementation, from a PyTorch net to a SymPy symbolic lambda expression). These two transformations are one-time transformations (for example, once \mathbf{f}_i has been transformed to a symbolic expression, `toSymbolic` cannot be applied to it again.) The `localSnap` transformation successively sets the incoming weights in the first layer to 0, thus favoring inputs that are closer to the current time step. The `integerSnap` transformation finds the (non-snapped) parameters in \mathbf{f}_i that is closest to an integer, and snaps it to that integer. The `rationalSnap` transformation finds the (non-snapped) parameter in \mathbf{f}_i that has the lowest bit sum when replaced by a rational number, as described in section IID, and snaps it to that rational number. The latter three transformations can be applied multiple times to \mathbf{f}_i , until there are no more parameters to snap in \mathbf{f}_i , or the transformation followed by fine-tuning fails to reduce the description length.

Algorithm 4 AI Physicist: Theory Unification

Require Hub: theory hub
Require K: initial number of clusters
1: **for** (\mathbf{f}_i, c_i) **in** `Hub.all-symbolic-theories` **do**
2: $\text{dl}^{(i)} \leftarrow \text{DL}(\mathbf{f}_i)$
3: **end for**
4: $\{S_k\} \leftarrow \text{Cluster } \{\mathbf{f}_i\}$ into K clusters based on $\text{dl}^{(i)}$
5: **for** S_k **in** $\{S_k\}$ **do**:
6: $(\mathbf{g}_{i_k}, \mathbf{h}_{i_k}) \leftarrow \text{Canonicalize}(\mathbf{f}_{i_k}), \forall \mathbf{f}_{i_k} \in S_k$
7: $\mathbf{h}_k^* \leftarrow \text{Mode of } \{\mathbf{h}_{i_k} | \mathbf{f}_{i_k} \in S_k\}$.
8: $G_k \leftarrow \{\mathbf{g}_{i_k} | \mathbf{h}_{i_k} = \mathbf{h}_k^*\}$
9: $\mathbf{g}_{\mathbf{p}_k} \leftarrow \text{Traverse all } \mathbf{g}_{i_k} \in G_k$ with synchronized steps,
 replacing the coefficient by a \mathbf{p}_{j_k} when not all
 coefficients at the same position are identical.
10: $\mathbf{f}_{\mathbf{p}_k} \leftarrow \text{toPlainForm}(\mathbf{g}_{\mathbf{p}_k})$
11: **end for**
12: $\mathcal{T} \leftarrow \{(\mathbf{f}_{\mathbf{p}_k}, \cdot)\}, k = 1, 2, \dots, K$
13: $\mathcal{T} \leftarrow \text{MergeSameForm}(\mathcal{T})$
14: **return** \mathcal{T}

subroutine Canonicalize (\mathbf{f}_i) :
s1: $\mathbf{g}_i \leftarrow \text{ToTreeForm}(\mathbf{f}_i)$
s2: $\mathbf{h}_i \leftarrow \text{Replace all non-input coefficient by a symbol } s$
return $(\mathbf{g}_i, \mathbf{h}_i)$

Appendix D: Unification algorithm

The unification process takes as input the symbolic prediction functions $\{(\mathbf{f}_i, \cdot)\}$, and outputs master theories $\mathcal{T} = \{(\mathbf{f}_{\mathbf{p}}, \cdot)\}$ such that by varying each \mathbf{p} in $\mathbf{p}_{\mathbf{p}}$, we can generate a continuum of prediction functions \mathbf{f}_i within a certain class of prediction functions. The symbolic expression consists of 3 building blocks: operators (e.g. $+, -, \times, /$), input variables (e.g. x_1, x_2), and coefficients that can be either a rational number or irrational number. The unification algorithm first calculates the DL $\text{dl}^{(i)}$ of each prediction function, then clusters them into K clusters using e.g. K-means clustering. Within each cluster S_k , it first canonicalizes each $\mathbf{f}_{i_k} \in S_k$ into a 2-tuple $(\mathbf{g}_{i_k}, \mathbf{h}_{i_k})$, where \mathbf{g}_{i_k} is a tree-form expression of \mathbf{f}_{i_k} where each internal node is an operator, and each leaf is an input variable or a coefficient. When multiple orderings are equivalent (e.g. $x_1 + x_2 + x_3$ vs. $x_1 + x_3 + x_2$), it always uses a predefined partial ordering. \mathbf{h}_{i_k} is the structure of \mathbf{g}_{i_k} where all coefficients are replaced by an s symbol. Then the algorithm obtains a set of \mathbf{g}_{i_k} that has the same structure \mathbf{h}_{i_k} with the largest cardinality (steps 7-8). This will eliminate some expressions within the cluster that might interfere with the following unification process. Step 9 is the core part, where it traverses each $\mathbf{g}_{i_k} \in G_k$ with synchronized steps using e.g. depth-first search or breath-first search. This is possible since each $\mathbf{g}_{i_k} \in G_k$ has the same tree structure \mathbf{h}_k^* . During traversing, whenever encountering a coefficient and not all coefficients across G_k at this position are the same, replace the coefficients by some symbol \mathbf{p}_{j_k} that has not

been used before. Essentially, we are turning all coefficients that varies across G_k into a parameter, and the coefficient that does not vary stays as it is. In this way, we obtain a master prediction function $\mathbf{f}_{\mathbf{p}_k}$. Finally, at step 13, the algorithm merges the master prediction functions in $\mathcal{T} = \{(\mathbf{f}_{\mathbf{p}_k}, \cdot)\}$ that have the exact same form, and return \mathcal{T} . The domain classifier is neglected during the unification process, since at different environments, each prediction function can have vastly different spacial domains. It is the prediction function (which characterizes the equation of motion) that is important for generalization.

Appendix E: Adding and Proposing theories

Here we detail the algorithms adding theories to the hub and proposing them for use in new environments. Alg. 6 provides a simplest version of the theory proposing algorithm. Given a new dataset D , the theory hub inspect all theories i , and for each one, counts the number n_i of data points where it outperforms all other theories. The top M_0 theories with largest n_i are then proposed.

For theory adding after training with differentiable-divide-and-conquer (Alg. 2), each theory i calculates its description length $\text{dl}^{(i)}$ inside its domain. If its $\text{dl}^{(i)}$ is smaller than a threshold η , then the theory (\mathbf{f}_i, c_i) with its corresponding examples $D^{(i)}$ are added to the theory hub. The reason why the data $D^{(i)}$ are also added to the hub is that $D^{(i)}$ gives a reference for how the theory (\mathbf{f}_i, c_i) was trained, and is also needed in the Occam's Razor algorithm.

Algorithm 5 AI Physicist: Adding Theories to Hub

Require Hub: theory hub
Require \mathcal{T} = $\{(\mathbf{f}_i, c_i)\}$: Trained theories from Alg. 2
Require Dataset D = $\{(\mathbf{x}_t, \mathbf{y}_t)\}$
Require η : DL threshold for adding theories to hub
1: $D^{(i)} \leftarrow \{(\mathbf{x}_t, \mathbf{y}_t) \mid \arg \max_j \{c_j(\mathbf{x}_t)\} = i\}, \forall i$
2: $\text{dl}^{(i)} \leftarrow \frac{1}{|D^{(i)}|} \sum_{(\mathbf{x}_t, \mathbf{y}_t) \in D^{(i)}} \ell_{\text{DL}, \epsilon}(\mathbf{f}_i(\mathbf{x}_t), \mathbf{y}_t), \forall i$
3: **for** i in $\{1, 2, \dots, |\mathcal{T}|\}$ **do**
4: **if** $\text{dl}^{(i)} < \eta$ **Hub.addIndividualTheory** $((\mathbf{f}_i, c_i), D^{(i)})$
5: **end for**

Algorithm 6 AI Physicist: Theory Proposing from Hub

Require Hub: theory hub
Require Dataset D = $\{(\mathbf{x}_t, \mathbf{y}_t)\}$
Require M_0 : number of theories to propose from the hub
1: $\{(\mathbf{f}_i, c_i)\} \leftarrow \mathbf{Hub.retrieve-all-theories}()$
2: $D_{\text{best}}^{(i)} \leftarrow \{(\mathbf{x}_t, \mathbf{y}_t) \mid \arg \min_j \ell_{\text{DL}, \epsilon}[\mathbf{f}_j(\mathbf{x}_t), \mathbf{y}_t] = i\}, \forall i$
3: $\mathcal{T}_{M_0} \leftarrow \{(\mathbf{f}_i, c_i) \mid D_{\text{best}}^{(i)} \text{ ranks among } M_0 \text{ largest sets in } \{D_{\text{best}}^{(i)}\}\}$
4: **return** \mathcal{T}_{M_0}

Appendix F: Proof of Theorem 1 and corollary

Here we give the proof for Theorem 1, restated here for convenience.

Theorem 1 Let $\hat{\mathbf{y}}_t^{(i)} \equiv \mathbf{f}_i(\mathbf{x}_t)$ denote the prediction of the target \mathbf{y}_t by the function \mathbf{f}_i , $i = 1, 2, \dots, M$. Suppose that $\gamma < 0$ and $\ell(\hat{\mathbf{y}}_t, \mathbf{y}_t) = \ell(|\hat{\mathbf{y}}_t - \mathbf{y}_t|)$ for a monotonically increasing differentiable function $\ell(u)$ that vanishes on $[0, u_0]$ for some $u_0 \geq 0$, with $\ell(u)^\gamma$ strictly convex for $u > u_0$.

Then if $0 < \ell(\hat{\mathbf{y}}_t^{(i)}, \mathbf{y}_t) < \ell(\hat{\mathbf{y}}_t^{(j)}, \mathbf{y}_t)$, we have

$$\left| \frac{\partial \mathcal{L}_\gamma}{\partial u_t^{(i)}} \right| > \left| \frac{\partial \mathcal{L}_\gamma}{\partial u_t^{(j)}} \right|, \quad (\text{F1})$$

where $u_t^{(i)} \equiv |\hat{\mathbf{y}}_t^{(i)} - \mathbf{y}_t|$.

Proof. Since $u_t^{(i)} \equiv |\hat{\mathbf{y}}_t^{(i)} - \mathbf{y}_t|$ and $\ell(\hat{\mathbf{y}}_t, \mathbf{y}_t) = \ell(|\hat{\mathbf{y}}_t - \mathbf{y}_t|)$, the generalized mean loss L_γ as defined in Eq. 3 can be rewritten as

$$\mathcal{L}_\gamma = \sum_t \left(\frac{1}{M} \sum_{k=1}^M \ell(u_t^{(k)})^\gamma \right)^{\frac{1}{\gamma}}, \quad (\text{F2})$$

which implies that

$$\begin{aligned} \left| \frac{\partial \mathcal{L}_\gamma}{\partial u_t^{(i)}} \right| &= \left| \frac{1}{\gamma M} \left(\frac{1}{M} \sum_{k=1}^M \ell(u_t^{(k)})^\gamma \right)^{\frac{1}{\gamma}-1} \frac{d\ell(u_t^{(i)})^\gamma}{du_t^{(i)}} \right| \\ &= \frac{1}{|\gamma| M} \left(\frac{1}{M} \sum_{k=1}^M \ell(u_t^{(k)})^\gamma \right)^{\frac{1}{\gamma}-1} \left| \frac{d\ell(u_t^{(i)})^\gamma}{du_t^{(i)}} \right|. \end{aligned}$$

Since only the last factor depends on i , proving equation (F1) is equivalent to proving that

$$\left| \frac{\partial \ell(u_t^{(i)})^\gamma}{\partial u_t^{(i)}} \right| > \left| \frac{\partial \ell(u_t^{(j)})^\gamma}{\partial u_t^{(j)}} \right|. \quad (\text{F3})$$

Let us henceforth consider only the case $u > u_0$, since the conditions $\ell(u_t^{(j)}) > \ell(u_t^{(i)}) > 0$ imply $u_t^{(j)} > u_t^{(i)} > u_0$. Since $\gamma < 0$, $\ell(u) > 0$ and $\ell'(u) \geq 0$, we have $\frac{\partial \ell(u)^\gamma}{\partial u} = \gamma \ell(u)^{\gamma-1} \ell'(u) < 0$, so that $\left| \frac{\partial \ell(u)^\gamma}{\partial u} \right| = -\frac{\partial \ell(u)^\gamma}{\partial u}$. Because $\ell(u)^\gamma$ is differentiable and strictly convex, its derivative $\frac{\partial \ell(u)^\gamma}{\partial u}$ is monotonically increasing, implying that $\left| \frac{\partial \ell(u)^\gamma}{\partial u} \right| = -\frac{\partial \ell(u)^\gamma}{\partial u}$ is monotonically decreasing. Thus $\left| \frac{d\ell(u_1)^\gamma}{du_1} \right| > \left| \frac{d\ell(u_2)^\gamma}{du_2} \right|$ whenever $u_1 < u_2$. Setting $u_1 = \ell(\hat{\mathbf{y}}_t^{(i)}, \mathbf{y}_t)$ and $u_2 = \ell(\hat{\mathbf{y}}_t^{(j)}, \mathbf{y}_t)$ therefore implies equation (F3), which completes the proof.

The following corollary 1.1 demonstrates that the theorem applies to several popular loss functions as well as our two description-length loss functions.

Corollary 1.1 Define $u \equiv |\hat{\mathbf{y}} - \mathbf{y}|$, the following loss functions which depend only on u satisfy the conditions for Theorem 1:

- $\ell(u) = u^r$ for any $r > 0$, which includes MSE loss ($r = 2$) and mean-absolute-error loss ($r = 1$).
- Huber loss: $\ell_\delta(u) = \begin{cases} \frac{1}{2}u^2, & u \in [0, \delta] \\ \delta(u - \frac{\delta}{2}), & \text{otherwise,} \end{cases}$ where $\delta > 0$
- Description length loss $\ell_{DL,\epsilon}(u) = \frac{1}{2} \log_2 \left(1 + \left(\frac{u}{\epsilon}\right)^2 \right)$
- Hard description length loss $\ell_{DLhard,\epsilon}(u) = \log_2 \max \left(1, \frac{u}{\epsilon} \right)$

Proof. (1) For $\ell(u) = u^r$, it is non-negative and $\ell(0) = 0$. The support for $\ell(u) > 0$ is $u > 0$. When $u > 0$, we have $\ell'(u) = pu^{r-1} > 0$. Furthermore, $\frac{\partial^2 \ell(u)^\gamma}{\partial u^2} = \gamma r(\gamma r - 1)u^{\gamma r - 2}$. Since $\gamma < 0, r > 0$, we have $\gamma r < 0$ and $\gamma r - 1 < 0$, and $\frac{\partial^2 \ell(u)^\gamma}{\partial u^2} = \gamma r(\gamma r - 1)u^{\gamma r - 2} > 0$ for $u > 0$. Thus $\ell(u)^\gamma$ is strictly convex on $u > 0$. Therefore, $\ell(u) = u^r$ with $r > 0$ satisfies the condition for Theorem 1.

(2) For Huber loss, it is non-negative and $\ell_\delta(0) = 0$. The support for $\ell_\delta(u) > 0$ is $u > 0$. When $u > 0$, we have

$$\ell'_\delta(u) = \begin{cases} u, & u \in (0, \delta] \\ \delta, & u \in (\delta, \infty) \end{cases}$$

which is always positive. Furthermore,

$$\frac{\partial^2 \ell_\delta(u)^\gamma}{\partial u^2} = \begin{cases} 2^{1-\gamma} \gamma (2\gamma - 1) u^{2\gamma - 2}, & u \in (0, \delta] \\ \delta^\gamma \gamma (\gamma - 1) (u - \frac{1}{2}\delta)^{\gamma - 2}, & u \in (\delta, \infty) \end{cases}$$

Since $\gamma < 0$, we have $\gamma(2\gamma - 1) > 0$ and $\gamma(\gamma - 1) > 0$. Therefore, in both cases $\frac{\partial^2 \ell_\delta(u)^\gamma}{\partial u^2} > 0$. Hence, $\ell_\delta(u)^\gamma$ is strictly convex when $u > 0$, satisfying the condition for Theorem 1.

(3) For the description length loss $\ell_{DL,\epsilon}(u) = \frac{1}{2} \log_2 \left(1 + \left(\frac{u}{\epsilon}\right)^2 \right)$, it is non-negative and $\ell_{DL,\epsilon}(0) = 0$, $\ell'_{DL,\epsilon}(u) = \frac{u}{\epsilon \left(1 + \left(\frac{u}{\epsilon}\right)^2\right)} > 0$ for $u > 0$. Therefore, $\ell_{DL,\epsilon}(u) = \ell_{DL,\epsilon}(0) + \int_0^u \ell'_{DL,\epsilon}(u) du > 0$ for $u > 0$. Hence, the support of $\ell_{DL,\epsilon}(u) > 0$ is $u > 0$, on which $\ell'_{DL,\epsilon}(u) > 0$.

Now let us prove that when $u > 0$, $\frac{\partial^2 \ell_{DL,\epsilon}(u)^\gamma}{\partial u^2} > 0$. For simplicity, define $\rho(u) \equiv \log_2(1 + u^2)$, we have $\ell_{DL,\epsilon}(u) = \frac{1}{2} \rho\left(\frac{u}{\epsilon}\right)$, and $\frac{\partial^2 \ell_{DL,\epsilon}(u)^\gamma}{\partial u^2} = \frac{1}{2\gamma\epsilon^2} \frac{\partial^2 \rho(u/\epsilon)^\gamma}{\partial u^2}$. Thus we only have to prove that $\frac{\partial^2 \rho(u)^\gamma}{\partial u^2} > 0$ always holds on $(0, \infty)$.

We have $\frac{\partial^2 \rho(u)^\gamma}{\partial u^2} = \frac{-2\gamma(\log(1+u^2))^{\gamma-2}}{(1+u^2)^2} \cdot (2u^2(1-\gamma) + (u^2-1)\log(1+u^2))$. The factor $\frac{-2\gamma(\log(1+u^2))^{\gamma-2}}{(1+u^2)^2}$ is always positive when $u > 0$. The other factor $2u^2(1-\gamma) + (u^2-1)\log(1+u^2) > 2u^2 + (u^2-1)\log(1+u^2)$ since $\gamma < 0$. Now we only have to prove that $\chi(u) \equiv 2u^2 + (u^2-1)\log(1+u^2) > 0$ when $u > 0$. We have $\chi(0) = 0$, $\chi'(u) = 2u\left(\frac{1+3u^2}{1+u^2} + \log(1+u^2)\right) > 0$ when $u > 0$. Therefore $\chi(u) = \chi(0) + \int_0^u \chi'(u) du > 0$ for $u > 0$. This completes the proof that $\frac{\partial^2 \ell_{DL,\epsilon}(u)^\gamma}{\partial u^2} > 0$ for $u > 0$, so $\ell_{DL,\epsilon}(u)^\gamma$ is strictly convex on $u > 0$. Above all, $\ell_{DL,\epsilon}(u)$ satisfies the condition for Theorem 1.

(4) For the hard description length loss $\ell_{DLhard,\epsilon}(u) = \log_2 \max \left(1, \frac{u}{\epsilon} \right)$, it is non-negative and $\ell_{DLhard,\epsilon}(0) = 0$. The support for $\ell_{DLhard,\epsilon} > 0$ is $u > \epsilon$. When $u > \epsilon$, $\ell'_{DLhard,\epsilon}(u) = \log_2\left(\frac{u}{\epsilon}\right)$, $\ell'_{DLhard,\epsilon}(u) = \frac{1}{u \ln 2} > 0$, and $\frac{\partial^2 \ell'_{DLhard,\epsilon}(u)}{\partial u^2} = \frac{(\ln(u/\epsilon))^{\gamma-2}}{u^2 \ln 2} \cdot \gamma(-1 + \gamma - \ln \frac{u}{\epsilon})$. The factor $\frac{(\ln(u/\epsilon))^{\gamma-2}}{u^2 \ln 2}$ is always positive when $u > \epsilon$. Also we have $-1 + \gamma - \ln \frac{u}{\epsilon} < 0$ for $u > \epsilon$ since $\gamma < 0$. Therefore, when $u > \epsilon$, $\frac{\partial^2 \ell'_{DLhard,\epsilon}(u)}{\partial u^2} > 0$, and $\ell'_{DLhard,\epsilon}(u)$ is strictly convex, satisfying the condition for Theorem 1.

Appendix G: Eliminating transition domains

In this appendix, we show how the only hard problem our AI Physicist need solve is to determine the laws of motion far from domain boundaries, because once this is done, the exact boundaries and transition regions can be determined automatically.

Our AI Physicist tries to predict the next position vector $\mathbf{y}_t \in R^d$ from the concatenation $\mathbf{x}_t = (\mathbf{y}_{t-T}, \dots, \mathbf{y}_{t-1})$ of the last T positions vectors. Consider the example shown in Figure 5, where motion is predicted from the last $T = 3$ positions in a space with $d = 2$ dimensions containing $n = 2$ domains with different physics (an electromagnetic field in the upper left quadrant and free motion elsewhere), as well as perfectly reflective boundaries. Although there are only two physics domains in the 2-dimensional space, there are many more types of domains in the $Td = 6$ -dimensional space of \mathbf{x}_t from which the AI Physicist makes its predictions of \mathbf{y}_t . When a trajectory crosses the boundary between the two spatial regions, there can be instances where \mathbf{x}_t contains 3, 2, 1 or 0 points in the first domain and correspondingly 0, 1, 2 or 3 points in the second domain. Similarly, when the ball bounces, there can be instances where \mathbf{x}_t contains 3, 2, 1 or 0 points before the bounce and correspondingly 0, 1, 2 or 3 points after. Each of these situations involves a different function $\mathbf{x}_t \mapsto \mathbf{y}_t$ and a corresponding 6-dimensional domain of validity for the AI Physicist to learn.

Our numerical experiments showed that the AI Physicist typically solves the big domains (where all vectors

in \mathbf{x}_t lie in the same spatial region), but occasionally fails to find an accurate solution in some of the many small transition domains involving boundary crossings or bounces, where data is insufficient. Fortunately, simple post-processing can automatically eliminate these annoying transition domains with an algorithm that we will now describe.

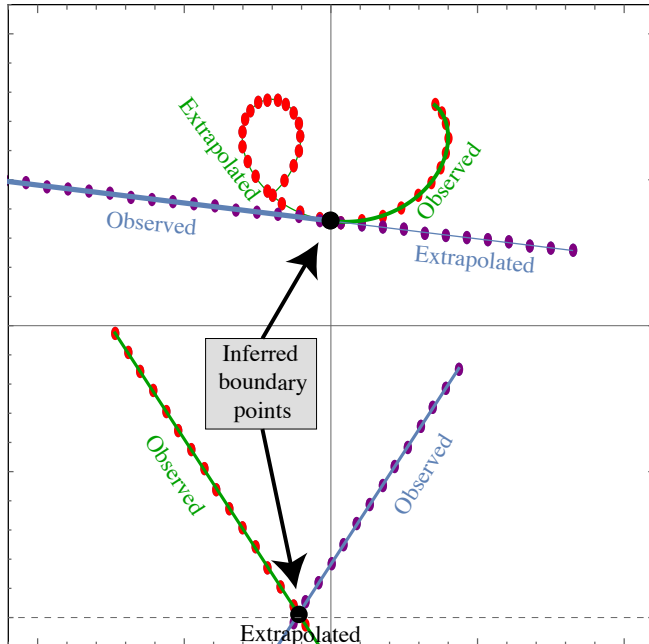


FIG. 5: Points where forward and backward extrapolations agree (large black dots) are boundary points. The tangent vectors agree for region boundaries (upper example), but not for bounce boundaries (lower example).

The first step of the algorithm is illustrated in Figure 5. For each big domain where our AI Physicist has discovered the future-predicting function $\mathbf{x}_t \mapsto \mathbf{y}_t$, we determine the corresponding function that predicts the *past* ($\mathbf{x}_t \mapsto \mathbf{y}_{t-T-1}$) by fitting to forward trajectories generated with random initial conditions. Now whenever a trajectory passes from a big domain through a transition region into a large domain, two different extrapolations can be performed: forward in time from the first big domain or backward in time from the second big domain. Using cubic spline interpolation, we fit continuous functions $\mathbf{y}_f(t)$ and $\mathbf{y}_b(t)$ (smooth curves in Figure 5) to these forward-extrapolated and backward-extrapolated trajectories, and numerically find the time

$$t_* \equiv \arg \min |\mathbf{y}_f(t) - \mathbf{y}_b(t)| \quad (\text{G1})$$

when the distance between the two predicted ball positions is minimized. If this minimum is numerically consistent with zero, so that $\mathbf{y}_f(t_*) \approx \mathbf{y}_b(t_*)$, then we record this as being a boundary point. If both extrapolations have the same derivative there, *i.e.*, if $\mathbf{y}'_f(t_*) \approx \mathbf{y}'_b(t_*)$, then it is an interior boundary point between two different regions (Figure 5, top), otherwise it is an external

boundary point where the ball bounces (Figure 5, bottom).

Figure 6 shows these two types of automatically computed boundary points in green and black, respectively. These can now be used to retrain the domain classifiers to extend the big domains to their full extent, eliminating the transition regions.

Occasionally the boundary point determinations fail because of multiple transitions within T time steps, Figure 6 illustrates that these failures (red dots) force us to discard merely a tiny fraction of all cases, thus having a negligible effect on the ability to fit for the domain boundaries.

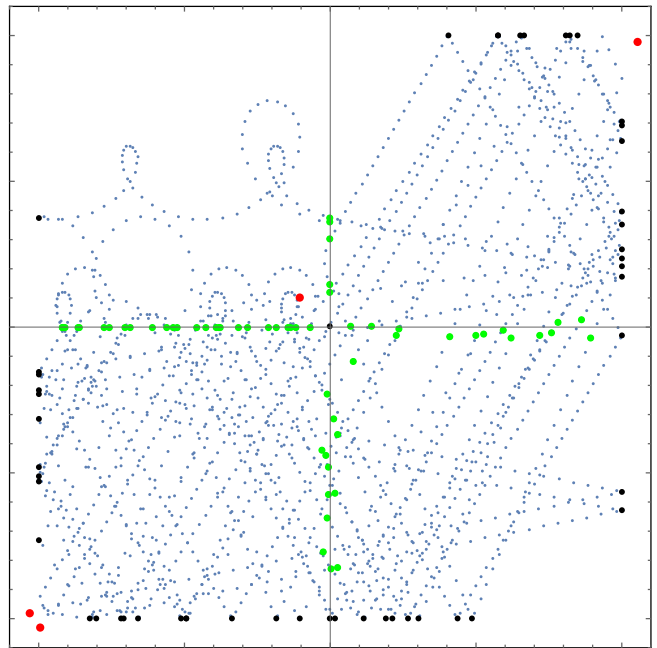


FIG. 6: Example of automatically determined boundary points.

Appendix H: Numerical experiment details

In this appendix, we provide supplementary details on our benchmark problems.

1. Mystery worlds

World generation Our mystery worlds consist of a ball elastically bouncing against the square boundary of the two-dimensional spatial region where $|x| \leq 2$ and $|y| \leq 2$ (see Figure 4). In each of the four quadrants, one of the following laws of physics are selected, together with their parameters sampled from distributions as follows:

1. Free motion
2. A uniform gravitational field $\mathbf{g} = \{g_x, g_y, 0\}$ with g_x, g_y drawn from a uniform distribution: $g_x, g_y \sim U[-5, 5]$.
3. Harmonic motion with frequency ω around a line a distance a from the origin, making an angle ϕ with the x -axis; $\omega \sim U[1, 4]$, $a \sim U[0.2, 0.5]$, $\phi \sim U[0, 2\pi]$.
4. A uniform electric field $\mathbf{E} = \{E_x, E_y, 0\}$ and magnetic field $\mathbf{B} = \{0, 0, B_z\}$; $E_x, E_y \sim U[-5, 5]$, $B_z \sim U[0, 10]$.

To control the difficulty of the tasks and avoid near-degenerate scenarios, we keep only mystery worlds satisfying the following two criteria: (1) At least 0.01 separation between all equations of motion (EOM) in the same world, defined as the Euclidean distance between the vectors of coefficients specifying the EOM difference equations, and (2) at least 0.0015 of any non-integer parameter from its nearest integer.

Trajectory simulation Within each world, we initialize the ball with a random position $(x, y) \sim U[-1, 1]^2$ and velocity $(v_0 \cos \theta_0, v_0 \sin \theta_0, 0)$; $v_r \sim U[0.1, 0.5]$, $\theta_0 \sim U[0, 2\pi]$. We then compute its position for $N = 4,000$ times steps $t = 1, 2, \dots, N$ with time interval 0.05.

Although the above-mentioned laws of physics are linear, the mapping from past points $(\mathbf{y}_{t-T}, \dots, \mathbf{y}_{t-1})$ to the next points \mathbf{y}_t is generally non-linear because of region boundaries where the ball either bounces or transitions to a different physics region. An exception is when three successive points lie within the same region (with the same physics), which happens far from boundaries: in this case, the mapping from $(\mathbf{y}_{t-2}, \mathbf{y}_{t-1}) \mapsto \mathbf{y}_t$ is deterministic and linear thanks to the differential equations of motion being second-order and linear.

Architecture For the newborn and AI Physicist agents, each prediction function \mathbf{f}_i is implemented as a three-layer neural net with linear activation, with two 8-neuron hidden layers. Each domain classifier c_i is implemented as a three-layer neural net, with two hidden 8-neuron layers with leakyReLU activation $\sigma(x) = \max\{0.3x, x\}$, and the output layer having linear activation. The baseline model is implemented as a single 3-layer neural net with two hidden 16-neuron layers with leakyReLU activation followed by a linear output layer. Note that for a fair comparison, the baseline model has more hidden neurons, to roughly compensate for the newborn and AI Physicist agents typically having multiple theories. The baseline network is nonlinear to boost its expressive power for modeling the nonlinear prediction function of each world as a whole. In both AI Physicist and Newborn, we set the initial number of theories $M = 4$. For the AI Physicist, the number of theories proposed from the theory hub $M_0 = 2$, to allow for both utilizing past experience and ability to learn new theories.

Evaluation The unsupervised classification accuracy it is defined as the fraction of correctly classified points, using the permutation of the learned domain labels that best matches the hidden ground truth domain labels. It is ‘‘unsupervised’’ in the sense that there is no supervision signal as to which domain label each point should be assigned to: the AI Physicist has to figure out the number of domains and their boundaries and assign each point to a domain, which is a difficult task.

We define a domain as *solved* if the agent discovers the its law of motion as difference equation (prediction function) within the following stringent tolerance: all rational coefficients in the difference equation are exactly matched, and all irrational coefficients agree to an accuracy better than 10^{-4} . Because of the nature of the physics problems, some of these difference equation coefficients take on the values 0, -1 , or 2, so solving a region requires successful integer snapping as described in Section IID. To make the problem even harder, we also fine-tune the magnetic field in five of the electromagnetic regions to make some of the coefficients simple fractions such as $1/3$ and $1/4$, thus making solving those regions contingent on successful rational snapping as described in Section IID. Domain solving can fail either by ‘‘undersnapping’’ (failing to approximate a floating-point number by a rational number) or ‘oversnapping’’ (mistakenly rounding to a rational number). All our mystery worlds can be downloaded at <http://space.mit.edu/aiphysicist.html>.

As shown in Appendix G, the only hard problem our AI Physicist or other algorithms need to solve is to determine the laws of motion away from domain boundaries. Therefore, we evaluate, tabulate and compare the performance of the algorithms only on interior points, *i.e.*, excluding data points $(\mathbf{x}_t, \mathbf{y}_t)$ straddling a boundary encounter.

2. Double pendulum

Our double pendulum is implemented as two connected pendulums with massless rods of length 1 and that each have a point charge of 1 at their end. As illustrated in Figure 7, the system state is fully determined by the 4-tuple $\mathbf{y} = (\theta_1, \dot{\theta}_1, \theta_2, \dot{\theta}_2)$ and immersed in a piecewise constant electric field \mathbf{E} : $\mathbf{E} = (0, -E_1)$ in the upper half plane $y \geq -1.05$, and $\mathbf{E} = (0, E_2)$ in the lower half plane $y < -1.05$, using coordinates where y increases vertically and the origin is at the pivot point of the upper rod.

We generate 7 environments by setting (E_1, E_2) equal to $(E_0, 2E_0)$, $(E_0, 1.5E_0)$, (E_0, E_0) , $(E_0, 0.5E_0)$, $(2E_0, E_0)$, $(1.5E_0, E_0)$, and $(0.5E_0, E_0)$, where $E_0 = 9.8$. We can see that there are two different EOMs for the double pendulum system depending on which of the two fields the lower charge is in (the upper charge is always in E_1). We use Runge-Kutta numerical integration to simulate $\mathbf{y} = (\theta_1, \dot{\theta}_1, \theta_2, \dot{\theta}_2)$ for 10,000 time steps with interval

Regions	log ₁₀ MSE			Classification accuracy			Unsolved domains			Description length		
	Base- line	New- born	AI phys	Base- line	New- born	AI phys	Base- line	New- born	AI phys	Base- line	New- born	AI phys
Free + gravity	-4.21	-14.02	-14.04	88.59%	100.00%	100.00%	2	0	0	11271.5	60.3	60.3
Free + gravity	-3.69	-14.03	-14.03	67.65%	100.00%	100.00%	2	0	0	11364.2	60.2	41.9
Free + gravity	-4.18	-13.98	-13.98	80.98%	100.00%	100.00%	2	0	0	11341.7	60.6	57.6
Free + gravity	-4.51	-14.06	-14.07	87.66%	100.00%	100.00%	2	0	0	11289.3	5.2	59.8
Free + harmonic	-3.77	-13.99	-13.94	73.54%	100.00%	100.00%	2	0	0	11333.8	94.4	139.9
Free + harmonic	-3.60	-14.05	-13.89	66.92%	100.00%	100.00%	2	0	0	11337.4	173.0	172.8
Free + harmonic	-3.77	-14.04	-13.95	59.46%	100.00%	100.00%	2	0	0	11317.5	156.0	173.8
Free + harmonic	-5.32	-10.48	-13.14	80.29%	100.00%	100.00%	2	1	0	11219.5	91.6	90.5
Free + harmonic	-3.64	-14.00	-13.89	71.70%	100.00%	100.00%	2	0	0	11369.6	143.7	136.6
Free + EM	-3.62	-13.95	-13.96	82.77%	100.00%	100.00%	2	0	0	11397.5	142.8	284.9
Free + EM	-4.13	-13.82	-13.67	76.55%	100.00%	100.00%	2	0	0	11283.0	306.2	306.2
Free + EM	-4.03	-13.45	-13.47	74.56%	99.97%	99.97%	2	0	0	11388.1	305.9	307.9
Free + EM	-4.31	-13.77	-13.62	86.68%	99.91%	99.91%	2	0	0	11257.7	152.0	133.5
Free + EM	-4.32	-14.00	-14.05	84.55%	100.00%	100.00%	2	0	0	11258.9	303.7	303.8
Free + EM rational	-3.45	-13.96	-13.95	77.88%	99.96%	99.93%	2	0	0	11414.9	194.2	195.8
Free + EM rational	-3.90	-13.96	-13.91	71.13%	100.00%	100.00%	2	0	0	11340.0	199.0	199.0
Free + EM rational	-4.12	-13.97	-13.90	72.78%	100.00%	100.00%	2	0	0	11330.7	198.8	198.8
Free + EM rational	-4.02	-14.07	-14.00	77.92%	100.00%	100.00%	2	0	0	11323.5	197.8	197.8
Free + EM rational	-4.83	-13.87	-13.86	91.14%	100.00%	100.00%	2	0	0	11247.1	10.3	13.9
Free + gravity + harmonic	-4.08	-14.03	-13.95	60.08%	100.00%	100.00%	3	0	0	11269.0	191.8	191.9
Free + gravity + harmonic	-4.31	-14.02	-13.66	63.01%	100.00%	100.00%	3	0	0	11334.2	170.4	83.1
Free + gravity + harmonic	-4.01	-14.01	-13.99	67.48%	100.00%	100.00%	3	0	0	11351.0	168.7	198.9
Free + gravity + harmonic	-3.64	-13.97	-13.88	60.02%	99.97%	99.93%	3	0	0	11374.6	225.7	225.7
Free + gravity + harmonic	-4.11	-7.42	-7.43	51.63%	100.00%	99.97%	3	1	1	11313.7	193.5	179.2
Free + gravity + EM	-3.79	-13.93	-13.47	57.89%	100.00%	100.00%	3	0	0	11334.0	323.9	346.8
Free + gravity + EM	-4.18	-14.00	-14.00	77.16%	100.00%	100.00%	3	1	1	11301.0	277.9	96.2
Free + gravity + EM	-3.38	-13.58	-13.87	53.33%	100.00%	99.96%	3	0	0	11381.4	360.4	364.0
Free + gravity + EM	-3.46	-13.87	-13.89	49.08%	100.00%	100.00%	3	0	0	11370.1	354.0	350.4
Free + gravity + EM	-3.54	-13.69	-13.83	51.28%	100.00%	100.00%	3	0	0	11370.3	331.1	320.7
Free + harmonic + EM	-3.87	-13.82	-13.55	67.27%	100.00%	100.00%	3	0	0	11404.0	267.1	275.4
Free + harmonic + EM	-3.69	-13.87	-10.93	56.02%	99.97%	99.94%	3	0	0	11413.4	468.5	464.9
Free + harmonic + EM	-4.06	-13.39	-13.56	70.87%	100.00%	100.00%	3	0	0	11340.0	452.3	452.3
Free + harmonic + EM	-3.46	-13.94	-10.51	59.02%	99.97%	99.93%	3	0	0	11416.0	475.5	471.9
Free + harmonic + EM	-3.70	-13.75	-13.82	61.67%	100.00%	100.00%	3	0	0	11354.9	466.8	466.8
Free + gravity + harmonic + EM	-3.76	-13.82	-9.48	27.93%	100.00%	99.94%	4	0	0	11358.8	526.9	530.4
Free + gravity + harmonic + EM	-3.74	-13.00	-13.18	40.80%	100.00%	99.97%	4	1	1	11284.8	418.5	389.1
Free + gravity + harmonic + EM	-4.09	-13.97	-13.75	35.69%	100.00%	100.00%	4	0	0	11297.4	504.6	504.6
Free + gravity + harmonic + EM	-3.63	-13.80	-9.99	31.61%	100.00%	99.97%	4	0	0	11407.4	526.3	526.2
Free + gravity + harmonic + EM	-3.51	-6.37	-13.52	32.97%	100.00%	100.00%	4	0	0	11445.8	527.4	527.5
Median	-3.89	-13.95	-13.88	67.56%	100.00%	100.00%	2.5	0.00	0.00	11338.7	198.9	198.9
Mean	-3.94	-13.44	-13.29	65.51%	99.99%	99.99%	2.6	0.10	0.07	11337.9	253.7	252.9

TABLE III: Results for each of our first 40 mystery world benchmarks, as described in the text. Each number is the best out of ten trials with random initializations (using seeds 0, 30, 60, 90, 120, 150, 180, 210, 240, 270), and refers to big domains only. Based on the “Unsolved domain” column, we count out of 40 worlds what’s the percentage Baseline, Newborn and AI Physicist completely solve (has unsolved domain of 0), which goes to the “Fraction of worlds solved” row in Table II.

of 0.05, and the algorithms’ task is to predict the future (\mathbf{y}_{t+1}) based on the past ($\mathbf{x}_t \equiv \mathbf{y}_t$; history length $T = 1$), and simultaneously discover the two domains and their different EOMs unsupervised.

In this experiment, we implement the Baseline and Newborn both as 6-layer neural net during DDAC. For the Newborn, each hidden layer has 160 neurons with hyperbolic tangent (tanh) activation, and for the Baseline, each hidden layer has 320 neurons with tanh activation for a fair comparison. For the Newborn, the optional AddTheories(\mathcal{T}, D) (step s9 in Alg. 2) is turned off to prevent unlimited adding of theories. The initial number M of theories for Newborn is set to $M = 2$ and $M = 3$, each run with 10 instances with random initialization.

Regions	Epochs to 10^{-2}			Epochs to 10^{-4}			Epochs to 10^{-6}			Epochs to 10^{-8}		
	Base- line	New- born	AI- phys	Base- line	New- born	AI physi	Base- line	New- born	AI phys	Base- line	New- born	AI phys
Free+gravity	100	85	85	8440	120	120	∞	4175	3625	∞	6315	4890
Free+gravity	100	70	10	4680	190	35	∞	2900	4650	∞	2995	6500
Free+gravity	85	100	15	∞	135	30	∞	8205	3815	∞	9620	6455
Free+gravity	95	75	20	7495	140	25	∞	6735	1785	∞	8040	2860
Free+gravity	110	75	0	1770	295	35	∞	3740	3240	∞	7030	3460
Free + harmonic	80	75	20	∞	145	25	∞	2725	4050	∞	2830	6145
Free + harmonic	85	75	20	∞	80	25	∞	7965	1690	∞	10000	3400
Free + harmonic	95	75	30	∞	110	30	∞	1805	3895	∞	1855	3900
Free + harmonic	25	20	5	1285	460	10	∞	5390	1060	∞	7225	6385
Free + harmonic	80	95	5	∞	110	20	∞	4380	3300	∞	4800	4035
Free + EM	90	85	20	∞	1190	115	∞	6305	3380	∞	6590	3435
Free + EM	125	120	0	6240	885	70	∞	7310	1865	∞	7565	1865
Free + EM	115	115	15	15260	600	70	∞	2430	1225	∞	2845	4435
Free + EM	145	90	0	6650	140	0	∞	3000	5205	∞	4530	8735
Free + EM	80	80	10	965	200	25	∞	4635	1970	∞	4690	2870
Free + EM rational	80	75	0	∞	580	70	∞	5415	4150	∞	5445	4175
Free + EM rational	100	100	10	∞	460	45	∞	2560	965	∞	2575	5760
Free + EM rational	140	95	10	11050	455	65	∞	1960	1150	∞	6295	4005
Free + EM rational	120	100	5	13315	325	175	∞	3970	1290	∞	4335	3560
Free + EM rational	35	30	35	1155	335	35	∞	3245	2130	∞	5115	5610
Free + gravity + harmonic	150	75	25	9085	130	30	∞	3870	6145	∞	5555	6185
Free + gravity + harmonic	145	90	5	6915	140	25	∞	4525	3720	∞	10275	4430
Free + gravity + harmonic	105	100	15	6925	155	40	∞	6665	6560	∞	8915	6845
Free + gravity + harmonic	95	95	5	∞	120	30	∞	5790	10915	∞	18450	13125
Free + gravity + harmonic	135	95	15	7970	190	45	∞	13125	7045	∞	∞	∞
Free + gravity + EM	130	100	20	∞	575	40	∞	3215	5095	∞	3215	5100
Free + gravity + EM	125	110	15	5650	160	30	∞	6085	4720	∞	8025	4980
Free + gravity + EM	80	65	15	∞	630	120	∞	4100	6250	∞	4100	6570
Free + gravity + EM	80	75	5	∞	90	45	∞	5910	5815	∞	7295	6090
Free + gravity + EM	80	85	20	∞	1380	465	∞	2390	11425	∞	7450	11510
Free + harmonic + EM	85	75	25	∞	600	150	∞	3775	4525	∞	4675	5070
Free + harmonic + EM	85	90	25	∞	1245	200	∞	6225	2340	∞	6390	3180
Free + harmonic + EM	115	85	15	16600	190	35	∞	6035	1515	∞	10065	2110
Free + harmonic + EM	80	70	35	∞	720	195	∞	6990	3895	∞	6995	6115
Free + harmonic + EM	85	65	10	∞	985	165	∞	5660	1670	∞	5820	1820
Free + gravity + harmonic + EM	90	75	0	∞	540	255	∞	8320	7390	∞	9770	7590
Free + gravity + harmonic + EM	95	80	15	∞	1265	635	∞	6520	6365	∞	8475	6475
Free + gravity + harmonic + EM	130	85	10	8620	575	105	∞	6320	4035	∞	9705	7685
Free + gravity + harmonic + EM	75	80	0	∞	815	425	∞	7575	8405	∞	10440	8620
Free + gravity + harmonic + EM	80	65	20	∞	735	280	∞	6715	4555	∞	12495	8495
Median	95	83	15	∞	330	45	∞	5403	3895	∞	6590	5100
Mean	98	82	15	∞	455	109	∞	5217	4171	∞	6892	5499

TABLE IV: Same as previous table, but showing number of training epochs required to reach various MSE prediction accuracies. We record the metrics every 5 epochs, so all the epochs are multiples of 5. Note that the AI Physicist has superceded 10^{-2} MSE already by 0 epochs for some environments, showing that thanks to the lifelong learning strategy which proposes previously learned theories in novel environments, reasonably good predictions can sometimes be achieved even without gradient descent training.

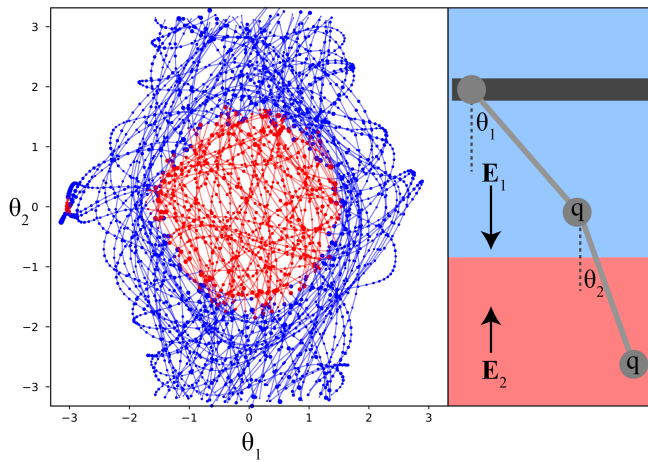


FIG. 7: In this mystery, a charged double pendulum moves through two different electric fields \mathbf{E}_1 and \mathbf{E}_2 , with a domain boundary corresponding to $\cos \theta_1 + \cos \theta_2 = 1.05$ (the approximately round region above left, where the lower charge crosses the \mathbf{E} -field boundary). The color of each dot represents the domain into which it is classified by a Newborn agent, and its area represents the description length of the error with which its position is predicted, for a precision floor $\epsilon \approx 0.006$. In this world, the Newborn agent has a domain prediction accuracy of 96.5%.

-
- [1] Y. LeCun, Y. Bengio, and G. Hinton, *Nature* **521**, 436 (2015).
- [2] P. W. Battaglia, J. B. Hamrick, V. Bapst, A. Sanchez-Gonzalez, V. Zambaldi, M. Malinowski, A. Tacchetti, D. Raposo, A. Santoro, R. Faulkner, et al., arXiv preprint arXiv:1806.01261 (2018).
- [3] S. Russell, D. Dewey, and M. Tegmark, *Ai Magazine* **36**, 105 (2015).
- [4] D. Amodei, C. Olah, J. Steinhardt, P. Christiano, J. Schulman, and D. Mané, arXiv preprint arXiv:1606.06565 (2016).
- [5] M. Boden, J. Bryson, D. Caldwell, K. Dautenhahn, L. Edwards, S. Kember, P. Newman, V. Parry, G. Pegman, T. Rodden, et al., *Connection Science* **29**, 124 (2017).
- [6] V. Krakovna and F. Doshi-Velez, arXiv preprint arXiv:1606.05320 (2016).
- [7] A. Graves, G. Wayne, and I. Danihelka, arXiv preprint arXiv:1410.5401 (2014).
- [8] S. Sukhbaatar, J. Weston, R. Fergus, et al., in *Advances in neural information processing systems* (2015), pp. 2440–2448.
- [9] S. Reed and N. De Freitas, arXiv preprint arXiv:1511.06279 (2015).
- [10] E. Parisotto, A.-r. Mohamed, R. Singh, L. Li, D. Zhou, and P. Kohli, arXiv preprint arXiv:1611.01855 (2016).
- [11] J. Devlin, J. Uesato, S. Bhupatiraju, R. Singh, A.-r. Mohamed, and P. Kohli, arXiv preprint arXiv:1703.07469 (2017).
- [12] N. Bramley, E. Schulz, F. Xu, and J. Tenenbaum (2018).
- [13] S. Muggleton, *New Generation Computing* **8**, 295 (1991), ISSN 1882-7055, URL <https://doi.org/10.1007/BF03037089>.
- [14] N. Lavrac and S. Dzeroski, in *WLP* (Springer, 1994), pp. 146–160.
- [15] P. Liang, M. I. Jordan, and D. Klein, in *Proceedings of the 27th International Conference on Machine Learning (ICML-10)* (2010), pp. 639–646.
- [16] K. Ellis, A. Solar-Lezama, and J. Tenenbaum, in *Advances in neural information processing systems* (2015), pp. 973–981.
- [17] E. Dechter, J. Malmaud, R. P. Adams, and J. B. Tenenbaum, in *IJCAI* (2013), pp. 1302–1309.
- [18] T. H. Cormen, C. E. Leiserson, R. L. Rivest, and C. Stein, *Introduction to algorithms* (MIT press, 2009).
- [19] J. Fürnkranz, *Artificial Intelligence Review* **13**, 3 (1999).
- [20] D. Ghosh, A. Singh, A. Rajeswaran, V. Kumar, and S. Levine, arXiv preprint arXiv:1711.09874 (2017).
- [21] S. Han, H. Mao, and W. J. Dally, arXiv preprint arXiv:1510.00149 (2015).
- [22] J. Rissanen, *Automatica* **14**, 465 (1978).
- [23] B. Hassibi and D. G. Stork, in *Advances in neural information processing systems* (1993), pp. 164–171.
- [24] K. Suzuki, I. Horiba, and N. Sugie, *Neural Processing Letters* **13**, 43 (2001).
- [25] P. D. Grünwald, I. J. Myung, and M. A. Pitt, *Advances in minimum description length: Theory and applications* (MIT press, 2005).
- [26] S. Han, J. Pool, J. Tran, and W. Dally, in *Advances in neural information processing systems* (2015), pp. 1135–1143.
- [27] J. Kirkpatrick, R. Pascanu, N. Rabinowitz, J. Veness, G. Desjardins, A. A. Rusu, K. Milan, J. Quan, T. Ramalho, A. Grabska-Barwinska, et al., *Proceedings of the national academy of sciences* p. 201611835 (2017).
- [28] Z. Li and D. Hoiem, *IEEE Transactions on Pattern Analysis and Machine Intelligence* (2017).
- [29] D. Lopez-Paz et al., in *Advances in Neural Information Processing Systems* (2017), pp. 6467–6476.
- [30] C. V. Nguyen, Y. Li, T. D. Bui, and R. E. Turner, arXiv preprint arXiv:1710.10628 (2017).
- [31] L. Blier and Y. Ollivier (2018).
- [32] J. Rissanen, *The Annals of statistics* pp. 416–431 (1983).
- [33] E. Real, S. Moore, A. Selle, S. Saxena, Y. L. Suematsu, J. Tan, Q. Le, and A. Kurakin, arXiv preprint arXiv:1703.01041 (2017).
- [34] B. Zoph and Q. V. Le, arXiv preprint arXiv:1611.01578 (2016).
- [35] B. Baker, O. Gupta, N. Naik, and R. Raskar, arXiv preprint arXiv:1611.02167 (2016).
- [36] M. Schmidt and H. Lipson, *science* **324**, 81 (2009).
- [37] D. P. Kingma and J. Ba, arXiv preprint arXiv:1412.6980 (2014).